

Reconstruction of Point Events in Liquid-Scintillator Detectors Subjected to Total Reflection

Wei Dou(窦威)^{a,b,c}, Benda Xu(续本达)^{*a,b,c,d,1}, Jianfeng Zhou(周建锋)^e,
Zhe Wang(王喆)^{a,b,c}, and Shaomin Chen(陈少敏)^{a,b,c}

^a*Department of Engineering Physics, Tsinghua University, Beijing, China*

^b*Center for High Energy Physics, Tsinghua University, Beijing, China*

^c*Key Laboratory of Particle & Radiation Imaging (Tsinghua University),
Ministry of Education, Beijing, China*

^d*Kavli Institute for the Physics and Mathematics of the Universe, UTIAS,
the University of Tokyo, Tokyo, Japan*

^e*Xingfan Information Technology Co., Ningbo, China*

September 23, 2022

Abstract

The outer water buffer is an economic option to shield the external radiative backgrounds for liquid-scintillator neutrino detectors. However, the consequential total reflection of scintillation light at the media boundary introduces extra complexity to the detector optics. This paper develops a precise detector-response model by investigating how total reflection complicates photon propagation and degrades reconstruction. We first parameterize the detector response by regression, providing an unbiased energy and vertex reconstruction in the total reflection region while keeping the number of parameters under control. From the experience of event degeneracy at the Jinping prototype, we then identify the root cause as the multimodality in the reconstruction likelihood function, determined by the refractive index of the buffer, detector scale and PMT coverage. To avoid multimodality, we propose a straightforward criterion based on the expected photo-electron-count ratios between neighboring PMTs. The criterion will be used to ensure success in future liquid-scintillator detectors by guaranteeing the effectiveness of event reconstruction.

KEYWORDS: event reconstruction, liquid scintillator, spherical harmonics, total reflection

*Corresponding author. orv@tsinghua.edu.cn

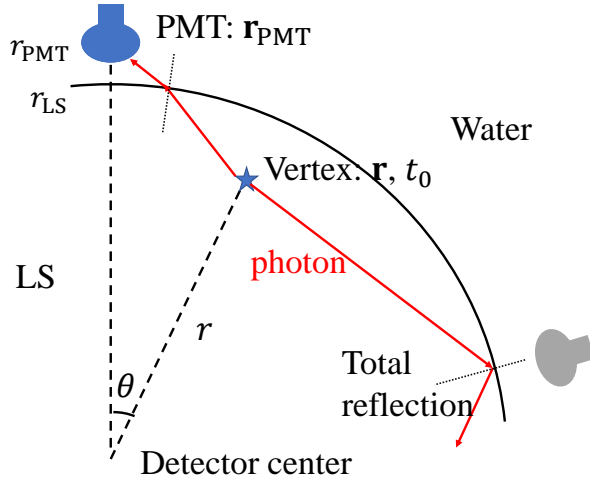


Figure 1: The particle deposits energy at position \mathbf{r} on time t_0 . The red lines are two typical photon tracks. Photons can reach the blue PMT directly but not the grey one due to TR. r_{LS} is the radius of the LS. The i -th PMT is located at position $\mathbf{r}_{\text{PMT},i}$ with $|\mathbf{r}_{\text{PMT},i}| = r_{\text{PMT}}$. A function of $(\mathbf{r}, \mathbf{r}_{\text{PMT},i})$ can be simplified to that of (r, θ) by spherical symmetry, where $r = |\mathbf{r}|$ and θ is the central angle defined by the vertex and the PMT.

1 Introduction

Liquid-scintillator (LS) detectors, such as Borexino [1], KamLAND [2], SNO+ [3] and JUNO [4], obtain lower energy thresholds and better energy resolutions than water Cherenkov detectors by enhanced light yields. It contains rich contemporary physics topics, including neutrino mass ordering [5, 6], neutrinoless double beta decay [7, 8, 9] as well as terrestrial, solar and supernova neutrinos [10].

The crucial step of energy reconstruction in LS detectors is to predict the *photon electron* (PE) count and timing on each *photomultiplier tube* (PMT) for a given vertex. Vertex reconstruction thus influences energy resolution. As illustrated in figure 1, if an LS detector is surrounded by a water buffer, each PMT can be blind to photons in a specific region due to *total reflection* (TR), causing a great challenge to vertex reconstruction.

The prevalent event reconstruction methods fall into 3 groups. *Barycenter* (BC) averages all PMT positions weighted by PE. It is biased but fast [11, 12, 13], often employed as the initial values to more advanced algorithms. *Maximum likelihood estimation* (MLE) uses predicted PE [14] or timing [11, 15, 16] or both [17, 18]. Its theoretical uncertainty is discussed by C. Galbiati et al [17]. The vertex reconstruction results are biased at the TR region if only use timing information [13]. Li [13] and Huang [19] predict PE using interpolation with a map to achieve unbiased results but introduce a high degree of freedom. Machine learning methods [20] such as neural networks and decision trees have good modeling power to describe TR optics but need high-quality labeled training datasets only available from detector simulations.

In this paper, we develop an improved MLE-based event reconstruction resilient to TR. Section 2 formulates a detector-response model and tests it with Monte Carlo (MC) simulation data. Section 3 analyzes the event degeneracy caused by the multimodality in the likelihood function. Section 4 shows the reconstruction performance. Finally, section 5 discusses the extensibility and limitation of our method. The symbol conventions for this paper are in

table 1.

Table 1: Definitions of symbols

variable	meaning (r.v. for random variable)	first appearance in section
E, t_0	visible energy and event start time	
$\mathbf{r}, \mathbf{r}_{\text{PMT}}$	vertex and PMT's position	2 Detector response by regression
i, j	PMT index and hit index	
$r_{\text{LS}}, r_{\text{PMT}}$	radii of the LS and PMT's position	
$r = \mathbf{r} $	vertex radius	2.1 PE and timing prediction
θ	central angle defined by PMT and vertex	
$\hat{E}, \hat{\mathbf{r}}$	reconstructed energy and position	4.1 Results from simulations
θ_{acr}	central angle defined by vertex and point of incidence to the acrylic shell	5.1 Other reflections by acrylic shell
n_i	observed PE on i th PMT	2 Detector response by regression
t_{ij}	observed j th hit's timing on i th PMT	
q_{ij}	reconstructed j th hit's charge on i th PMT	4.2 Results from raw data
N_{PMT}	number of PMTs	3.1 Cosine distance
N_{hit}	total hit number	4.1 Results from simulations
$\lambda_i, \lambda_i(r, \theta)$	predicted PE on i th PMT	2 Detector response by regression
$T_i, T_i(r, \theta)$	predicted timing on i th PMT	
$c_l^\lambda, c_l^\lambda(r)$	l th PE coefficient	2.1 PE and timing prediction
$c_l^T, c_l^T(r)$	l th timing coefficient	
$c_{l,m}^\lambda, c_{l,m}^T$	PE and timing coefficient	
μ_i, U_i	PE and timing PMT-specific offset	
P_l	Legendre polynomial	
$\psi(t)$	scintillation time profile	2 Detector response by regression
$R^0(t)$	timing PDF by $\psi(t)$ and TTS, etc.	
\mathcal{L}	likelihood function	2.1 PE and timing prediction
$\mathcal{R}_\tau, \mathcal{R}_\tau(t)$	loss function using τ -quantile	
$R(t)$	quantile regression approximation to $R^0(t)$	
τ, t_s	quantile value and time scale	
τ_r, τ_d	rise and decay time constant	
D_{KL}	Kullback-Leibler divergence	4.2 Results from raw data
Λ	PE pattern	3.1 Cosine distance
d_{cos}	cosine distance	
$C_{1r}(\mathbf{r})$	contour function	3.2 Cosine distance for 3-PMT case
Ω	solid angle	
β	angle of incidence on a PMT	

2 Detector response by regression

This section develops a model to predict the PE and timing in an LS detector that is suitable for TR. The radius of the LS is r_{LS} . Figure 1 shows how a typical LS detector works. An ionizing particle begins to deposit energy E at the position \mathbf{r} on time t_0 . It produces scintillation

photons, each obeying a scintillation *time profile* $\psi(t)$. PMTs are located at position \mathbf{r}_{PMT} with $|\mathbf{r}_{\text{PMT}}| = r_{\text{PMT}}$. A photon travels to a PMT with *time of flight* (TOF) and induces a PE with the probability of *quantum efficiency* (QE). The PE gets amplified by a series of dynodes inside the PMT with *transit time* (TT), whose *spread* is TTS. The whole process is called an *event*.

The event is characterized by PE counts n_i and timings t_{ij} extracted from the waveforms on the i th PMT, where $j \in \mathbb{N}$ and $j < n_i$. Throughout this paper, we use *PE* to be the short for ‘‘PE counts’’. *Detector response model* predicts the PE λ_i and timing T_i . λ_i is the average of the Poissonian n_i . T_i is a shift to the t_{ij} ’s *probability distribution function* (PDF) $R^0(t - T_i)$, which is determined by t_0 , TOF, TT and $\psi(t)$.

2.1 PE and timing prediction

λ_i and T_i are the functions of $(\mathbf{r}, \mathbf{r}_{\text{PMT}})$. If the detector is spherically symmetric, the function can be rewritten in (r, θ) . Here r is the vertex radius and θ is the central angle defined by PMT and vertex. By *varying coefficient model* [21], we fit the conditional distribution of θ given r , then fit the coefficients with r by the method of least squares.

In the first step, n_i is modeled by Poisson regression [22] as count data. λ_i is connected to the observation n_i by the Poisson log-likelihood

$$\log \mathcal{L} = - \sum_i \lambda_i + \sum_i n_i \log \lambda_i + \text{Const.} \quad (1)$$

A logarithm, called a *link function* in generalized linear model [22] terminology, connects λ_i with the predictor variable as a linear combination of Legendre polynomials $P_l(\cos \theta)$. l is the order and $c_l^\lambda(r)$ ’s are the regression coefficients.

$$\lambda_i(r, \theta_i) = \mathbb{E}[n_i | r, \theta_i] = \exp \left\{ \sum_l c_l^\lambda(r) P_l(\cos \theta_i) + \log E + \mu_i \right\} \quad (2)$$

Here E is the energy, μ_i is the correction term to match the PMT-specific differences dominated by QE. We restrict $\sum_i \mu_i = 0$, E and μ_i enter the regression as offsets. Eqs. (1) and (2) models the dependence on θ_i and outputs a set of r -dependent coefficients $c_l^\lambda(r)$.

Similarly, quantile regression [23] is used to model timing, reducing the influence of the heavy tail of $R^0(t - T_i)$. The predicted T_i for the τ -quantile is

$$T_i(r, \theta_i) = \arg \min_c \left[\sum_j \mathcal{R}_\tau(t_{ij} - c) \right] = \sum_l c_l^T(r) P_l(\cos \theta_i) + U_i + t_0, \quad (3)$$

where $\mathcal{R}_\tau(t)$ is the loss function defined by

$$\mathcal{R}_\tau(t) = \begin{cases} -t(1 - \tau) & , \text{ if } t < 0; \\ t\tau & , \text{ if } t \geq 0. \end{cases} \quad (4)$$

t_0 is the time offset and U_i is the PMT-specific offset dominated by TT with $\sum_i U_i = 0$. Like $c_l^\lambda(r)$, $c_l^T(r)$ encodes the θ dependence of timing.

Minimizing $\mathcal{R}_\tau(t)$ in eqs. (3) and (4) is equivalent to maximizing a likelihood function $\mathcal{L} \propto \exp(-\mathcal{R}_\tau/t_s)$, where t_s is an arbitrary positive real number encoding a *time scale*. The

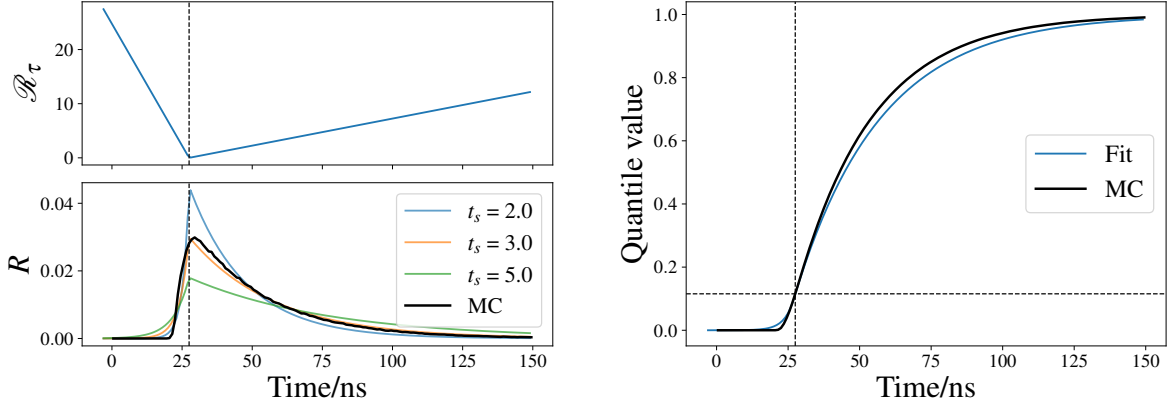
normalizing constant is

$$\int_{-\infty}^{\infty} \exp\left(-\frac{\mathcal{R}_\tau(t)}{t_s}\right) dt = \frac{t_s}{1-\tau} + \frac{t_s}{\tau} = \frac{t_s}{\tau(1-\tau)} \quad (5)$$

Therefore, quantile regression approximates the timing PDF $R^0(t)$ by

$$R(t) = \frac{\tau(1-\tau)}{t_s} \exp\left(-\frac{\mathcal{R}_\tau(t)}{t_s}\right). \quad (6)$$

The examples of the loss function $\mathcal{R}_\tau(t)$ and timing PDF $R(t)$ are shown in figure 2a.



(a) The shape of \mathcal{R}_τ (top) and R (bottom)

(b) The CDF of $R(t - T_i)$

Figure 2: (a) shows the $\mathcal{R}_\tau(t - T_i)$ (top) and $R(t - T_i)$ (bottom). T_i is 27.5 ns and τ is 0.1. “MC” represents $R^0(t)$. It is the histogram of simulated event timings at the detector center, see section 2.2. The best t_s is 3.0 ns. (b) is the *cululative distribution function* (CDF) of $R^0(t)$ as “MC” and $R(t - T_i)$ as “Fit”. The steepest slope is at the peak of $R^0(t)$, leading to $\tau \approx 0.1$.

In the second step, we use another set of Legendre polynomials to fit coefficients $c_l^\lambda(r)$ and $c_l^T(r)$. r is scaled to $[-1, 1]$ by dividing the LS radius r_{LS} . Due to the symmetry, we only use the even orders to guarantee the $c_l^\lambda(r)$ and $c_l^T(r)$ ’s derivatives are 0 at the detector center,

$$c_l^\lambda(r) = \sum_{m=0}^{\infty} c_{l,2m}^\lambda P_{2m}(r/r_{\text{LS}}), \quad c_l^T(r) = \sum_{m=0}^{\infty} c_{l,2m}^T P_{2m}(r/r_{\text{LS}}). \quad (7)$$

The above varying coefficient model requires simulation or calibration at fixed radii. Alternatively, if the simulated events are uniformly distributed in the detector, the above 2-step requirement can be relaxed with a one-step regression,

$$\lambda_i(r, \theta_i) = \exp\left[\sum_m c_m^\lambda F_m(r, \cos \theta_i)\right], \quad T_i(r, \theta_i) = \sum_m c_m^T F_m(r, \cos \theta_i). \quad (8)$$

$F_m(r, \cos \theta)$ is a binary basis function of r and θ at the m th order such as Zernike polynomials [24]. Another way to construct a binary basis function is to product the two Legendre polynomials from the varying coefficient model, called *double Legendre*.

$$F_{l,m}(r, \cos \theta) = P_m(r/r_{\text{LS}}) \times P_l(\cos \theta) \quad (9)$$

which is indexed by two subscripts l and m . Due to the memory constraints of our computing system, a regression cannot handle more than 800 parameters in one pass. Consequently binary basis models are more restricted than the varying coefficient one, although the former models more symmetrically handle r and θ . Their best order selections are discussed in section 2.2.

2.2 Training and validation

The training dataset is generated by a custom piece of software, *Jinping Simulation and Analysis Package* (JSAP), based on GEANT4 [25]. Two geometries are defined as in figure 3: the first utilizes the *Jinping prototype* [26], featuring 30 PMTs, and the second is an *ideal detector* upgraded to 120 PMTs, following the Fibonacci arrangement [27]. The number of PMTs in the ideal detector follows the criterion in section 3.3. The central LS [28] is in an acrylic shell with a water buffer. The Jinping prototype has an outlet and a support base, which are removed in the ideal detector. Table 2 lists some essential parameters. In reality, the QE and TT for each PMT are different, and the TTS affects $R^0(t)$. We ignore such difference since $\psi(t)$ dominates the $R^0(t)$. μ_i in eq. (1) and U_i in eq. (3) can be obtained by calibration. Without loss of generality, we assume PMTs are identical by setting $\mu_i = U_i = 0$.

Table 2: Important parameters in simulation

parameter	value (Jinping prototype)	value (ideal detector)	parameter	value
r_{LS}	650 mm	650 mm	QE	0.2
r_{PMT}	832 mm	900 mm	TTS	2.2 ns
number of PMTs	30	120	t_0	0 ns

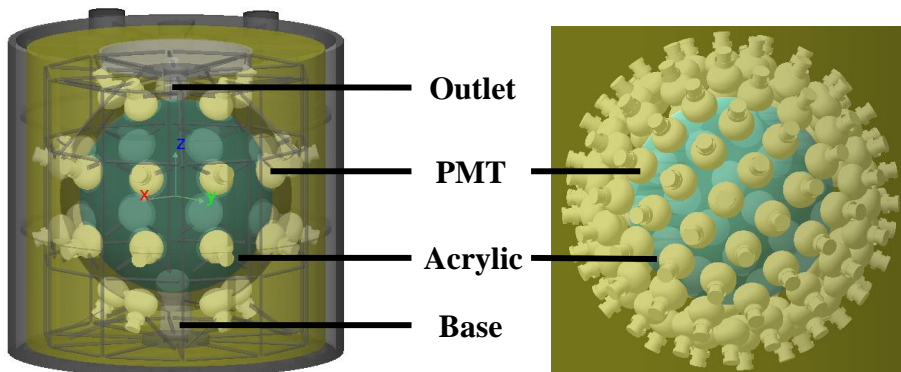


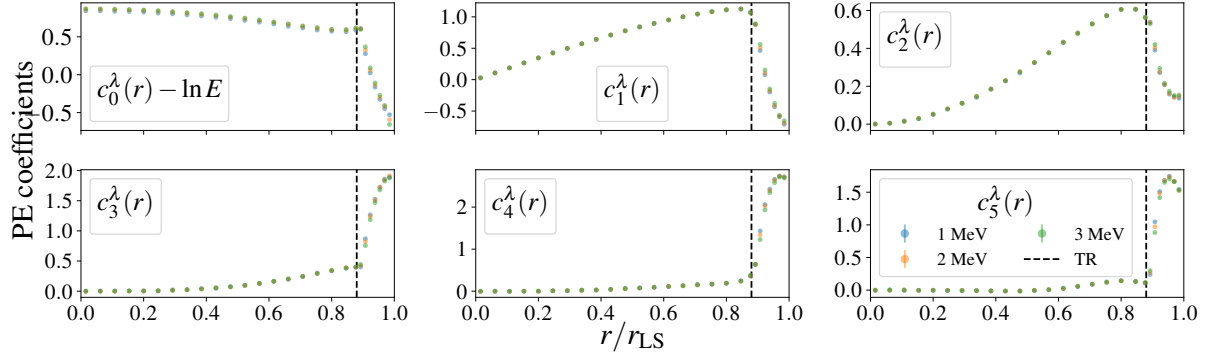
Figure 3: Geometries of the Jinping prototype (left) and the ideal detector (right).

$\psi(t)$ is parameterized in eq. (10) by the *decay time constant* $\tau_d = 26.0$ ns and the *rise time constant* $\tau_r = 1.6$ ns,

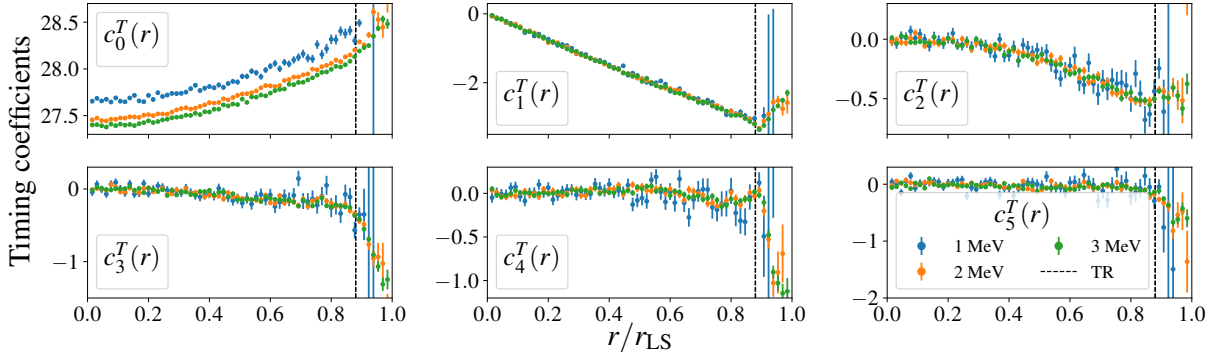
$$\psi(t) \sim \exp\left(-\frac{t}{\tau_d}\right) \left[1 - \exp\left(-\frac{t}{\tau_r}\right)\right]. \quad (10)$$

The average refraction index of LS is 1.48, causing TR to occur at $r > 0.88r_{\text{LS}}$ which is 570 mm for the Jinping prototype.

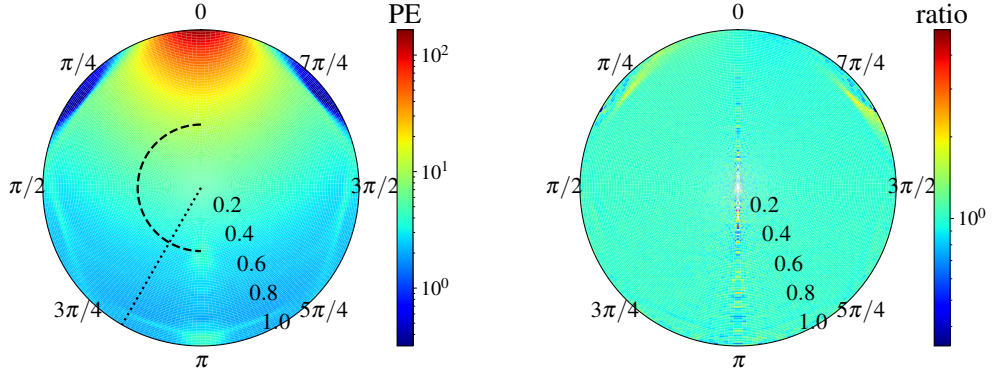
We focus on e^- in this work. The training dataset includes multiple batches. Vertices in each batch have the same r , ranging from 0 mm to 550 mm with step 10 mm, and from 550 mm to 640 mm with step 2 mm. Figure 4a subtracts $\log E$ in the 0th order and the first six orders of c_l^λ under 1, 2 and 3 MeV. Figure 4b shows the first six orders of c_l^T . The coefficient



(a) First six $c_l^\lambda(r)$ of Jinping prototype under different energies.

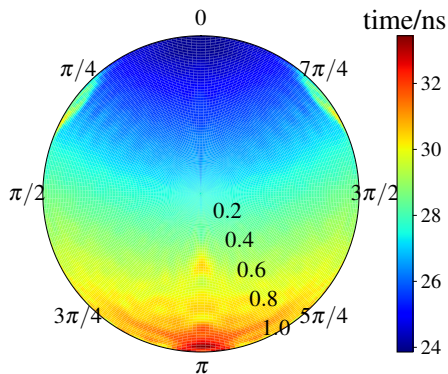


(b) First six $c_l^T(r)$ of Jinping prototype under different energies.

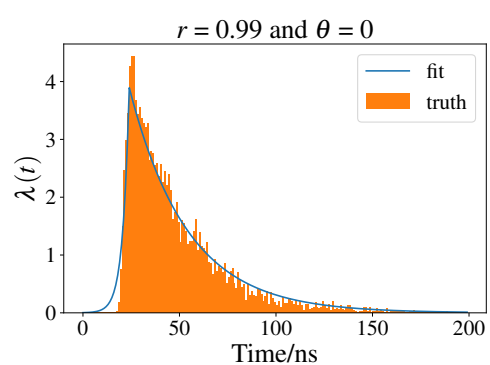


(c) Predicted PE

(d) Ratio of simulation over predicted PEs



(e) Predicted timing



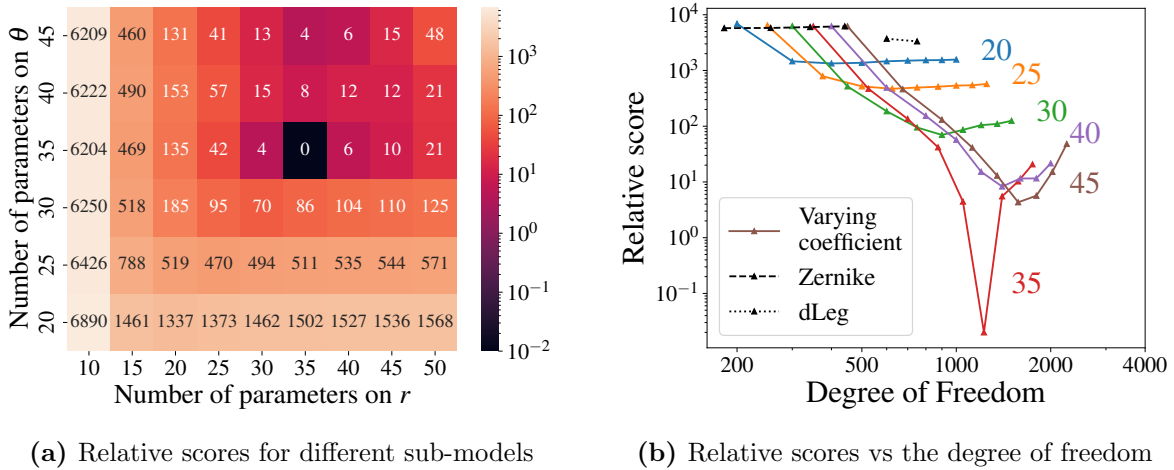
(f) Inhomogeneous Poisson process

Figure 4: (a) and (b) are regression results. TR occurs at the $0.88r_{\text{LS}}$ (dashed line). The error bars are ± 1 standard deviations. (c) – (f) uses 2 MeV e^- in Jinping prototype. (c) and (e) are the PE and timing responses, respectively. In (c), we shall look into the focus structures in the slices of the dashed line $r = 0.4r_{\text{LS}}$ and dotted line $\theta = 5\pi/6$ in section 5.1. (d) is the ratio between the predicted PE and its MC truth. (f) shows the average function of the inhomogeneous Poisson process compared with the MC at $r = 0.99r_{\text{LS}}$ and $\theta = 0$.

changes dramatically at $0.88r_{\text{LS}}$, where the TR just happens. It is evident from figure 4a and 4b that c_l^λ and c_l^T depend on energy only when $l = 0$. Therefore one energy sample alone captures the detector response in any other energies. The Jinping prototype utilizes a 25-PMT threshold [29] and the trigger efficiency drops for events near the boundary. We take 2 MeV events that are energetic enough to guarantee $\sim 100\%$ trigger efficiency.

We can express $\lambda_i(r, \theta_i)$ and $T_i(r, \theta_i)$ in a single heat map of a disk. Figure 4c and 4e shows the predicted PE and timing, respectively. The ratio of the predicted PE and its truth is almost 1 in figure 4d, showing a good fit. The models of PE and timing at a specific r, θ can be combined into an inhomogeneous Poisson process with average function $\lambda_i(r, \theta_i)R(t - T_i(r, \theta_i))$, shown in figure 4f.

To determine the optimal number of parameters, we simulate another 15000 events as the validation dataset. A better goodness of fit for PE is manifested by a higher score in log-likelihood given by eqs. (1) and (7). Figure 5a shows the highest score requires the number of parameters to be 35×35 of (θ, r) . The binary polynomials are shown for comparison in figure 5b. The number of parameters is up to 441 for Zernike and 750 for double Legendre polynomials. Their scores are limited by the number of parameters.



(a) Relative scores for different sub-models

(b) Relative scores vs the degree of freedom

Figure 5: Relative scores to the best model. (a) indicates the number of parameters 35×35 of (θ, r) to be the best. (b) adds the binary polynomials. The numbers are the number of parameters on θ in the varying coefficient models. “Zernike” and “dLeg” are Zernike and double Legendre polynomials, respectively.

It is difficult to make a similar selection for $c_{l,m}^T$ because their scores rely on τ and t_s . Since PE is dominant in the small detectors [17], we choose 10×35 on (θ, r) for $c_{l,m}^T$ to balance speed and accuracy.

2.3 Likelihood for reconstruction

We use MLE for reconstruction with the likelihood function satisfying

$$\log \mathcal{L}(\mathbf{r}, E, t_0) \sim \underbrace{\sum_i \sum_j \frac{\mathcal{R}_\tau(t_{ij} - T_i - t_0)}{t_s}}_{\text{timing part}} + \underbrace{\sum_i \left(-\frac{E\lambda_i}{E_0} + n_i \log \frac{E\lambda_i}{E_0} \right)}_{\text{PE part}}. \quad (11)$$

The former is the timing part and the latter is the PE part. E only contributes to the PE part. E_0 is energy (2 MeV) in the training dataset. The unbiased energy estimation of eq.

(11) is

$$\frac{\partial \log \mathcal{L}}{\partial E} = 0 \Rightarrow \hat{E} = \frac{\sum_i n_i}{\sum_i \lambda_i(\mathbf{r})} E_0 \quad (12)$$

We use *Sequential Least Squares Programming* [30] to maximize eq. (11). The energy is calculated in each iteration by eq. (12) to reduce the time costs.

Most gradient-based methods are local optimizers. The origin of the local maxima will be discussed in section 3. Our strategy to obtain the global maximum is as follows. We generate two grids to calculate the predicted PE. Each grid is $30 \times 50 \times 50$ equally spaced on r , $\cos \theta_v$ and ϕ_v . The inner grid covers the radius of 0 mm to 570 mm and the outer covers the rest. We choose the best points of the inner and outer grids as initial values for the gradient optimizer. The larger of the two $\log \mathcal{L}$'s is recorded.

3 Multimodality of the likelihood function

The convexity of the minus-log-likelihood in eq. (11) is crucial for reconstruction. The reconstruction results are sensitive to the initial values of the gradient optimizer if the minus-log-likelihood is not convex, or equivalently, the likelihood function is *multimodal*. Using a poor vertex undermines the energy resolution and the background rejection by fiducial volume cuts.

In this section, we concentrate on PE (but not timing) since it is dominant in the small detectors [17]. We replace the likelihood function in eq. (11) with *cosine distance* to eliminate the influence of fluctuations in the observed PEs. We further narrow our focus to the 3 closest PMTs, giving a criterion of multimodality in the likelihood function.

3.1 Cosine distance

We define *pattern* Λ as a vector containing the predicted PE on the PMT space.

$$\Lambda = \{\lambda_1, \lambda_2, \dots, \lambda_{N_{\text{PMT}}}\} \quad (13)$$

If \mathbf{r}_1 and \mathbf{r}_2 are both the solution for an event and $\mathbf{r}_1 \neq \mathbf{r}_2$, we have $\Lambda(\mathbf{r}_1) = \alpha \Lambda(\mathbf{r}_2)$, and α is an arbitrary positive number. The *cosine distance*

$$d_{\text{cos}}[\Lambda(\mathbf{r}_1) | \Lambda(\mathbf{r}_2)] = 1 - \frac{\Lambda(\mathbf{r}_1) \cdot \Lambda(\mathbf{r}_2)}{\|\Lambda(\mathbf{r}_1)\| \|\Lambda(\mathbf{r}_2)\|} \quad (14)$$

is zero.

d_{cos} matches well with the $-\log \mathcal{L}$. Figure 6a shows an event at (0, 0, 100) mm of the Jinping prototype. Two local solutions with different initial values are shown in black dashed lines. The green line scans the $-\log \mathcal{L}$ between the two. The blue line shows the d_{cos} of these points by the true expected PEs. Figure 6b and 6c are at (540, 0, 0) mm in the ideal detector. Figure 6b demonstrates a good unimodal event, in which both d_{cos} and $-\log \mathcal{L}$ are convex. Figure 6c is an example of multimodal event where $-\log \mathcal{L}$ is not convex, but the d_{cos} is the same as figure 6b. Observation fluctuations lead to the $-\log \mathcal{L}$ difference between the two. Of all events at (540, 0, 0) mm, the fraction of bad events like figure 6c is less than 1%.

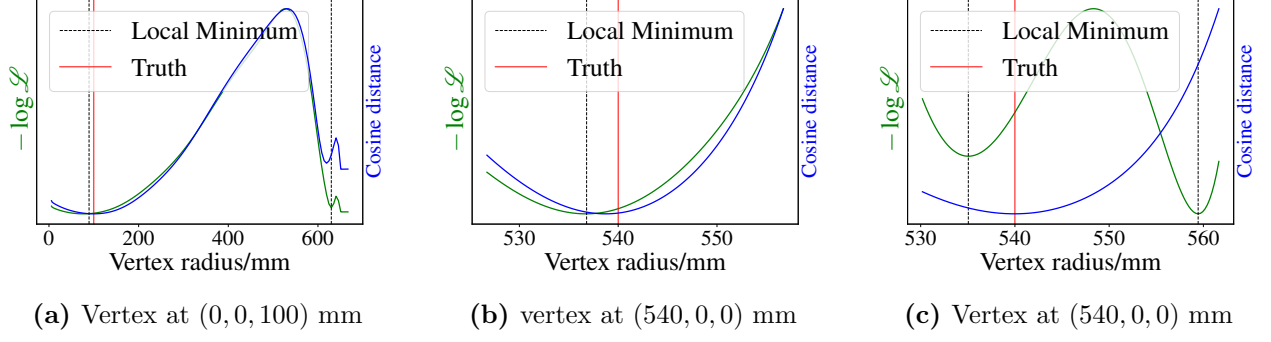


Figure 6: Comparison of d_{\cos} with $-\log \mathcal{L}$. All events at $(0, 0, 100)$ mm degenerate with $r = 600$ mm on the z axis. (a) is one typical event and the two local solutions are in black dashed lines. The true vertex is in the red line. The green line scans the $-\log \mathcal{L}$ and the blue line scans the d_{\cos} , showing that they both have two local minima. (b) and (c) use true events at $(540, 0, 0)$ mm, comparing one unimodal with one multimodal event. d_{\cos} itself is convex. The difference in $-\log \mathcal{L}$ between (b) and (c) is from fluctuations.

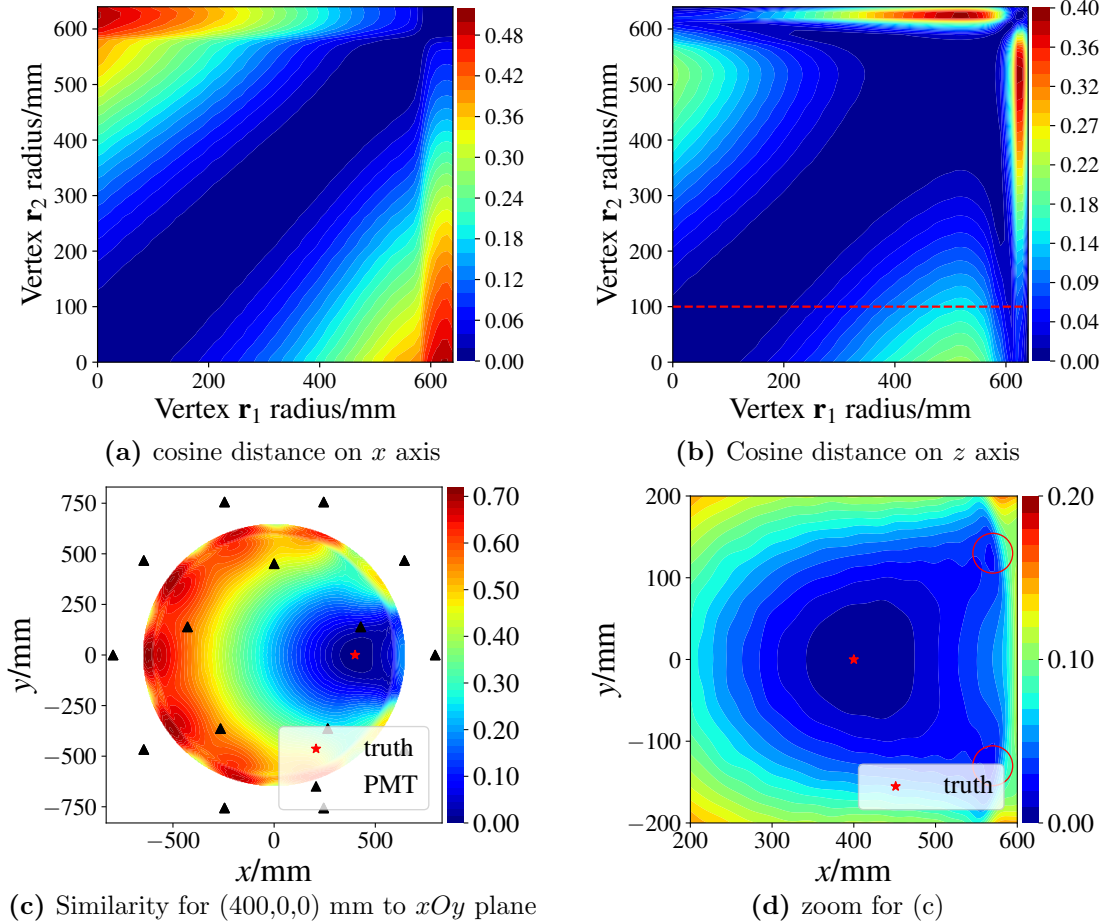


Figure 7: Cosine distance of different cases. The color shows the value of $d_{\cos}[\Lambda(\mathbf{r}_1) | \Lambda(\mathbf{r}_2)]$. (a) \mathbf{r}_1 and \mathbf{r}_2 are both on the x axis. (b) \mathbf{r}_1 and \mathbf{r}_2 are both on the z axis. The red dashed line shows the center and radius at 600 mm degenerate. (c) \mathbf{r}_1 is $(400, 0, 0)$ mm and \mathbf{r}_2 scans the xOy plane. (d) is the zoom for (c). The red star and the red circles degenerate.

Figure 7 maps out multimodality of d_{\cos} . \mathbf{r}_1 and \mathbf{r}_2 are all on the x axis in figure 7a, and on the z axis in figure 7b. The slice in figure 7b shows $z = 0$ mm and 600 mm degenerate. In figure 7c, \mathbf{r}_1 is 400 mm on the x axis and \mathbf{r}_2 scans the xOy plane. Figure 7d zooms around the true position. Local minima are found near the detector boundary. The shape of d_{\cos} map is remarkably consistent with the reconstruction results in figure 10, which will be discussed in section 4.1.

3.2 Cosine distance for 3-PMT case

Observing that closer PMTs contribute more to the likelihood function, we only consider the three closest PMTs to the vertex for simplicity. Considering symmetry, in figure 8 the vertices are constrained in the shadow region without loss of generality. We define the *contour function* by

$$C_{1i}(\mathbf{r}) = \frac{\lambda_1(\mathbf{r})}{\lambda_i(\mathbf{r})}, \quad (15)$$

where $\lambda_1(\mathbf{r})$ is the expected number of PEs at the closest PMT to \mathbf{r} , and $\lambda_i(\mathbf{r})$ is that of the 2nd or 3rd closest PMT with $i = 2$ or 3 respectively. In a two-dimensional slice of the detector, a certain value of $C_{1i}(\mathbf{r})$ defines an *equivalent ratio* (ER) line. If one ER line of C_{12} and another in C_{13} has two intersections \mathbf{r}_1 and \mathbf{r}_2 , $d_{\cos}[\Lambda(\mathbf{r}_1) | \Lambda(\mathbf{r}_2)] \approx 0$. Because the 3 dominating PMTs satisfies $\lambda_1(\mathbf{r}_1) : \lambda_2(\mathbf{r}_1) : \lambda_3(\mathbf{r}_1) = \lambda_1(\mathbf{r}_2) : \lambda_2(\mathbf{r}_2) : \lambda_3(\mathbf{r}_2)$. Therefore it is the key to count the intersections between any pair of C_{12} and C_{13} ER lines.

We study the multimodality affected by angle of incidence β for *homogeneous materials* and TR for *inhomogeneous materials* respectively. In the former case, the LS and the buffer have the same refractive index. Assuming the PMTs are small enough and their surface is flat, the predicted PE λ_i is proportional to the solid angle Ω_i . Ω_i is subtended by the i th PMT from the vertex,

$$\lambda_i(\mathbf{r}) \propto \Omega_i(\mathbf{r}) \propto \frac{1}{\|\mathbf{r} - \mathbf{r}_{\text{PMT},i}\|_2^2} \cos \beta_i, \quad (16)$$

where \mathbf{r} , $\mathbf{r}_{\text{PMT},i}$ are defined in figure 1. β is the angle of incidence on a PMT. Eq. (16) well describes TAO [31] to be equipped with SiPM and XMASS [32] with flat-photocathode R10789 PMTs [33]. To comparatively study the effect by β_i by leaving it out,

$$\lambda_i(\mathbf{r}) \propto \Omega_i(\mathbf{r}) \propto \frac{1}{\|\mathbf{r} - \mathbf{r}_{\text{PMT},i}\|_2^2}. \quad (17)$$

We set $r_{\text{PMT}} = r_{\text{LS}}$, namely no buffer is installed between LS and PMTs. The PMTs located at 0, $2\pi/3$ and $4\pi/3$ directions are indexed by 1, 2 and 3. C_{12} and C_{13} are symmetric. Figure 8b demonstrates the ER lines with β and figure 8a demonstrates those without. The two intersections circled red in figure 8b show that β leads to multimodality.

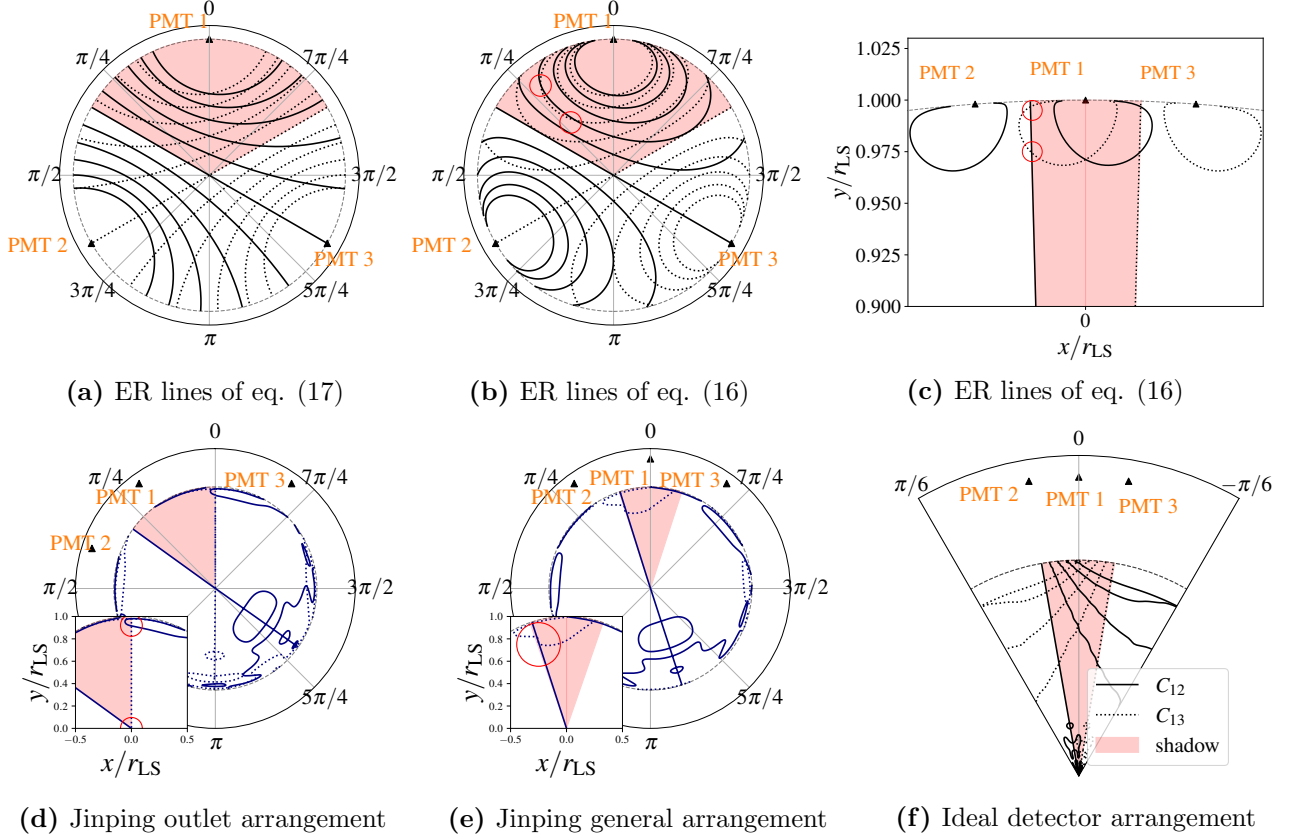


Figure 8: ER lines of different detector response models. PMTs are in black triangles. (a) – (c) are the homogeneous materials with $r_{\text{PMT}} = r_{\text{LS}}$. For (a) and (b), PMTs are arranged at $0, 2\pi/3, 4\pi/3$. For (c), PMTs are arranged at $0, \pm\pi/100$. (d) – (f) are the inhomogeneous materials, using the coefficients shown in figure 4c. (d) is the outlet direction, PMTs are arranged at $2\pi/5$ and $\pm\pi/5$, lacking at 0 . The intersections of $C_{12} = 1$ and $C_{13} = 1$ are at the central and top regions. (e) is the general direction. PMTs are arranged at 0 and $\pm\pi/5$. More than one intersections of $C_{12} = 1$ and $C_{13} = 4.5$ are at 350 mm and 550 mm. (f) is the ideal detector without multimodality. PMTs are arranged at $0, \pm\pi/18$. For all subfigures, the vertices are constrained in the shadow region. We circle the multiple intersections of ER lines in (b), (c), (d) and (e).

To account for the suspicion that multimodality is induced by sparse PMT arrangement in figure 8b, consider two intersections with a more compact arrangement under eq. (16) in figure 8c. Regardless of the PMT arrangement, the shadow boundary is not only an ER line but also the bisector of the two neighboring PMTs. The point on the bisector at $r = r_{\text{LS}}$ is always one of the intersections under eq. (16). PMT is almost blind to this point due to a large β . To avoid this, a non-fluorescent buffer is necessary to isolate scintillation events away from the PMTs.

We use *inhomogeneous materials* to study the TR effect. The buffer's refractive index is different from the central detector. For the Jinping prototype, we see from the fitted model that TR makes ER lines segmented. A two-dimensional slice of the Jinping prototype includes 10 PMTs. We pick the 3 PMTs at $(0, \pm\pi/5)$ to represent the *general direction* in figure 8e, matching figure 7d. It is evident from figure 8e that events at 350 mm and 550 mm degenerate. We also pick $(\pm\pi/5, 2\pi/5)$ as the *outlet direction* in figure 8d, matching figure 7b. Vertices at $z = 600$ mm and the center degenerate. Such 3-PMT plots are reasonable simplifications to reproduce the trends of d_{cos} in all-PMT cases.

The ER lines near the TR region are distorted compared to the homogeneous materials. The rich functional structures in this region are a hotbed to multimodality. A solution is to reduce the gaps between PMTs, making them close enough so as not to fall into each other's TR regions. For example, the ideal detector has no multiple intersections in ER lines in figure 8f.

3.3 A criterion against multimodality

In figure 8a, the predicted PE is approximately proportional to the inverse square of the distance from the vertex to PMT. The incident angle and the TR break that trend. These effects are so strong that the closest PMTs could receive fewer PEs, making the ER lines distorted and intersect multiple times. They are the seeds to multimodality. Therefore a perfect inverse-squared detector in figure 8a is always free from multimodality.

Taking λ_1 and λ_2 to be the same meaning as eq. (15), in figures 8b and 8c, adding buffer is equivalent to reducing λ_1 . Conditions of figures 8d and 8e improve by reducing the gap between neighboring PMTs, making λ_2 larger. The two phenomena can be unified by λ_1/λ_2 : for any event, $\lambda_1/\lambda_2 < 10$ is required to avoid multimodality.

It is sufficient to examine if an extreme vertex with the biggest λ_1/λ_2 is less than 10. Such an extreme vertex is approximately realized in the center-PMT direction at $r = r_{LS}$, illustrated in figure 9a. Note that $\lambda_1/\lambda_2 < 10$ is a necessary condition, we might construct some case where the TR region is fully contained in the gap between 2 PMTs to embed a lot of degeneracy but still satisfies $\lambda_1/\lambda_2 < 10$. λ_1 and λ_2 is related to the r_{LS} , r_{PMT} , N_{PMT} and the buffer's refractive index.

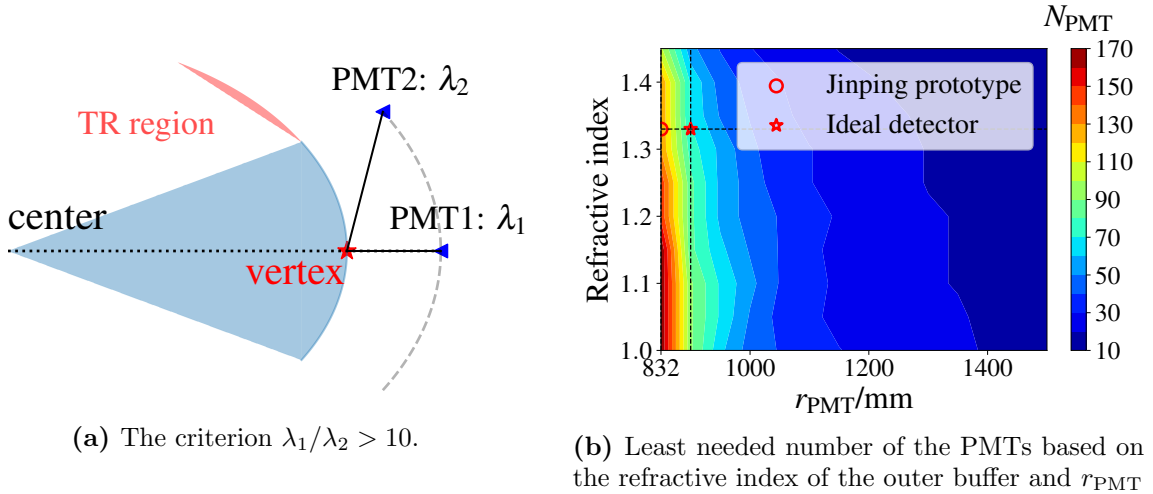


Figure 9: (a) shows the criterion to avoid multimodality. λ_1/λ_2 should be less than 10 and the TR region should be excluded. (b) shows the least number of needed PMTs. r_{LS} is fixed to 645 mm. For the Jinping prototype, the average refractive index of the water is 1.33 and r_{PMT} is 832 mm, showing that at least 120 PMTs are necessary. The red star is the ideal detector with $r_{PMT} = 900$ mm, requiring at least 90 PMTs. The larger the r_{PMT} , the refractive index and the number of PMTs help to avoid multimodality.

Keeping an identical distance between neighboring PMTs to extend our criterion to three dimensions, $N_{PMT,3D}$ scales approximately as $N_{PMT,2D}^2/3$. Fixing $r_{LS} = 650$ mm, figure 9b shows the least needed number of PMTs under different r_{PMT} and the buffer refractive index.

For a certain N_{PMT} , larger r_{PMT} or the refractive index gives better resilience against degeneracy. For $r_{\text{PMT}} = 832$ mm and the refractive index 1.33, 120 PMTs are needed. Using 8-inch PMTs, the PMT coverage, calculated by $N_{\text{PMT}} \times (10\text{mm})^2 / 4r_{\text{PMT}}^2$, should exceed 40%. Be aware that the larger r_{PMT} leads to poorer PMT coverage, thus r_{PMT} should be as close to the lower limit in figure 9b as possible. r_{PMT} 's other influences will be discussed in section 5.1.

The ideal detector with $r_{\text{PMT}} = 832$ mm requires at least 90 PMTs. To reduce the influences of fluctuations, we use 120 PMTs to guarantee perfect reconstruction performance.

4 Reconstruction results

We verify our vertex reconstruction on MC and raw data. For MC, we use the Jinping prototype to verify the conditions of multimodality in section 3.3, and the ideal detector to study the reconstruction bias and resolution. The simulations use 2 MeV e^- on x and z axes: x represents the general direction, and z the outlet direction, aligned with the definitions in section 3.2. For raw data, we analyze the ^{214}Bi - ^{214}Po cascade signals by the model fitted from the Jinping-prototype simulation.

4.1 Results from simulations

We compare the results using MLE and BC. For BC, the reconstructed vertex $\hat{\mathbf{r}}$ is

$$\hat{\mathbf{r}} = 1.5 \times \frac{\sum_i q_i \mathbf{r}_{\text{PMT},i}}{\sum_i q_i} \quad (18)$$

and the energy is scaled from the total number of hits,

$$\frac{\hat{E}}{[\text{MeV}]} = \frac{N_{\text{hit}}}{65} \quad (19)$$

where 1.5 is a correction factor and 65 is the average total PE at 1 MeV at the Jinping prototype. The simulation data ranges from 0 mm to 650 mm with steps of 10 mm. Each step contains 5000 events.

Figure 10a shows a reasonable vertex reconstruction in the general direction. That is in contrast to the outlet direction in figure 10c, where events at the detector center and around (0, 0, 600) mm are indistinguishable. Similarly, events at 350 mm and 550 mm degenerate. Such degeneracy is a consequence of multimodality in the likelihood function as discussed in section 3.3. Notice that the d_{cos} relations in figures 7a and 7b predict the major patterns of MLE reconstructions in figures 10a and 10c.

In figures 10b and 10d, similar worsen trends appear for BC from the general to the outlet direction. They both have severe biases.

For the ideal detector, no outlet is considered. x and z axes are equivalent. MLE performs well without degeneracy in figures 10g and 10i, proving the effectiveness of the $\lambda_1/\lambda_2 < 10$ criteria in section 3.3. BC, on the contrary, still reconstructs badly in the TR region. Our detector model in section 2 describes the TR region well and consequently MLE provides a big improvement upon the BC method.

The energy reconstruction for the Jinping detector is shown in figure 10e and 10f. The scaled total PE decreases rapidly in the TR region, which introduces a big bias. The reconstructed energy by MLE is even worse, due to the wrong vertices. The true vertices give an

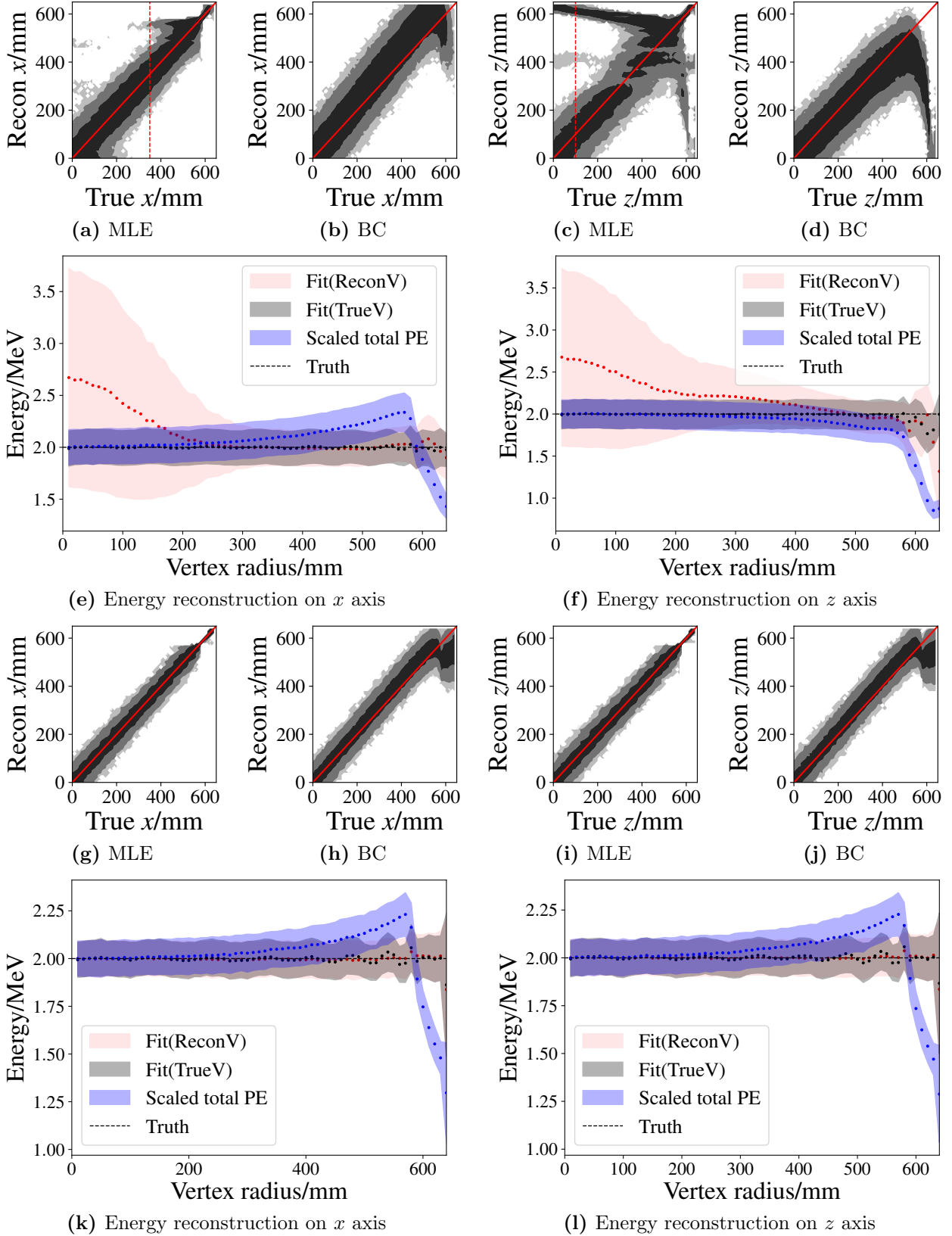


Figure 10: Vertex and energy reconstruction performance of 2 MeV e^- . (a) – (f) are from the Jiniping prototype. The red dashed lines in (a) and (c) show the degeneracies. (g) – (l) are from the ideal detector. In (a) – (d) and (g) – (j), the light grey, grey and black represent bins with 1–10, 10–100 and > 100 events, respectively. (e), (f) and (k), (l) are the energy reconstruction results of 2 MeV e^- on the Jiniping prototype and the ideal detector. “Fit(ReconV)” and “Fit(TrueV)” are energies with reconstructed and true vertices, respectively. “Scaled total PE” is by eq. (19).

unbiased energy estimation, indicating that the detector response model is accurate. For the ideal detector of figure 10k and 10l, BC has similar trends. The MLE is almost unbiased and improved by eliminating the vertex degeneracy.

Excluding the regions $|\hat{\mathbf{r}}| > 600$ mm and $\sqrt{\hat{x}^2 + \hat{y}^2} < 50$ mm, the standard deviation of Jinping prototype is 60 mm at the center and 20 mm in the TR region. The energy reconstruction heavily depends on the vertex. When using the true vertex, the results are almost unbiased even in the TR region. The energy resolution of the Jinping prototype is approximately $11\%/\sqrt{E[\text{MeV}]}$.

4.2 Results from raw data

The raw data of the Jinping prototype is the PMT waveform $w_i(t)$, which is a convolution of hits $\sum_j \delta(t - t_{ij})$ and the *single PE response* $V_{\text{PE}}(t)$,

$$w_i(t) = \sum_j \delta(t - t_{ij}) \otimes V_{\text{PE}}(t) + \epsilon(t) = \sum_j V_{\text{PE}}(t - t_{ij}) + \epsilon(t), \quad (20)$$

$\epsilon(t)$ is Gaussian white noise. We use *Richardson-Lucy direct demodulation* (LucyDDM) for deconvolution [34]. The input is the timing series t_{ij} , returning the gain modified charge q_{ij} . Traditional LucyDDM is biased in photon density due to an artificial threshold. Xu et al. [35] use a rescaling factor to significantly reduce the bias. In terms of the photon density resolution, LucyDDM matches the fit method [35] and consumes less time.

Xu et al. [35] also utilize the non-normalized Kullback-Leibler (KL) divergence [36, 37] for reconstruction, which is a special case of *density power divergence* [37]. It joins the waveform analysis results $\sum_j q_{ij} \delta(t - t_{ij})$ and the inhomogeneous Poisson process. We take the non-normalized KL divergence as the pseudo-minus-log-likelihood in this work.

$$\begin{aligned} -\log \mathcal{L}(E, \mathbf{r}, t_0) &= \sum_i D_{\text{KL}} \left[\sum_j q_{ij} \delta(t - t_{ij}) \middle| E \lambda_i(r, \theta_i) R(t - t_0 - T_i(r, \theta_i)) \right] \\ &= - \sum_i \left[\sum_j q_{ij} \log R(t_{ij} - t_0 - T_i) + \left(\sum_j q_{ij} \right) \log(E \lambda_i) - E \lambda_i \right] + \text{Const.} \\ &\sim \underbrace{\sum_i \sum_j q_{ij} \frac{-\mathcal{R}_\tau(t_{ij} - T_i - t_0)}{t_s}}_{\text{timing part}} + \underbrace{\sum_i [-q_i \log(E \lambda_i) + E \lambda_i]}_{\text{PE part}}, \end{aligned} \quad (21)$$

where $q_i = \sum_j q_{ij}$.

The detector response model is based on simulation since there is no dedicated calibration runs [29]. We check the ^{214}Bi - ^{214}Po cascade signal of e^- prompt and α delayed. The cuts are listed below:

1. $|\hat{\mathbf{r}}_{\text{prompt}}| < 600$ mm and $|\hat{\mathbf{r}}_{\text{delay}}| < 600$ mm,
2. $\sqrt{\hat{x}_{\text{prompt}}^2 + \hat{y}_{\text{prompt}}^2} > 50$ mm and $\sqrt{\hat{x}_{\text{delay}}^2 + \hat{y}_{\text{delay}}^2} > 50$ mm,
3. Visible energy of e^- is less than 3.5 MeV,
4. Visible energy of α is in 0.7 MeV to 1 MeV,
5. Delayed time between the prompt and delayed signal in 10 us to 1000 us,
6. $|\hat{\mathbf{r}}_{\text{prompt}} - \hat{\mathbf{r}}_{\text{delay}}| < 300$ mm.

Figures 11a, 11b, 11c and 11d show data distribution of the six cuts except the 3rd, 4th, 5th and 6th, respectively. The cut is colored red in each subfigure.

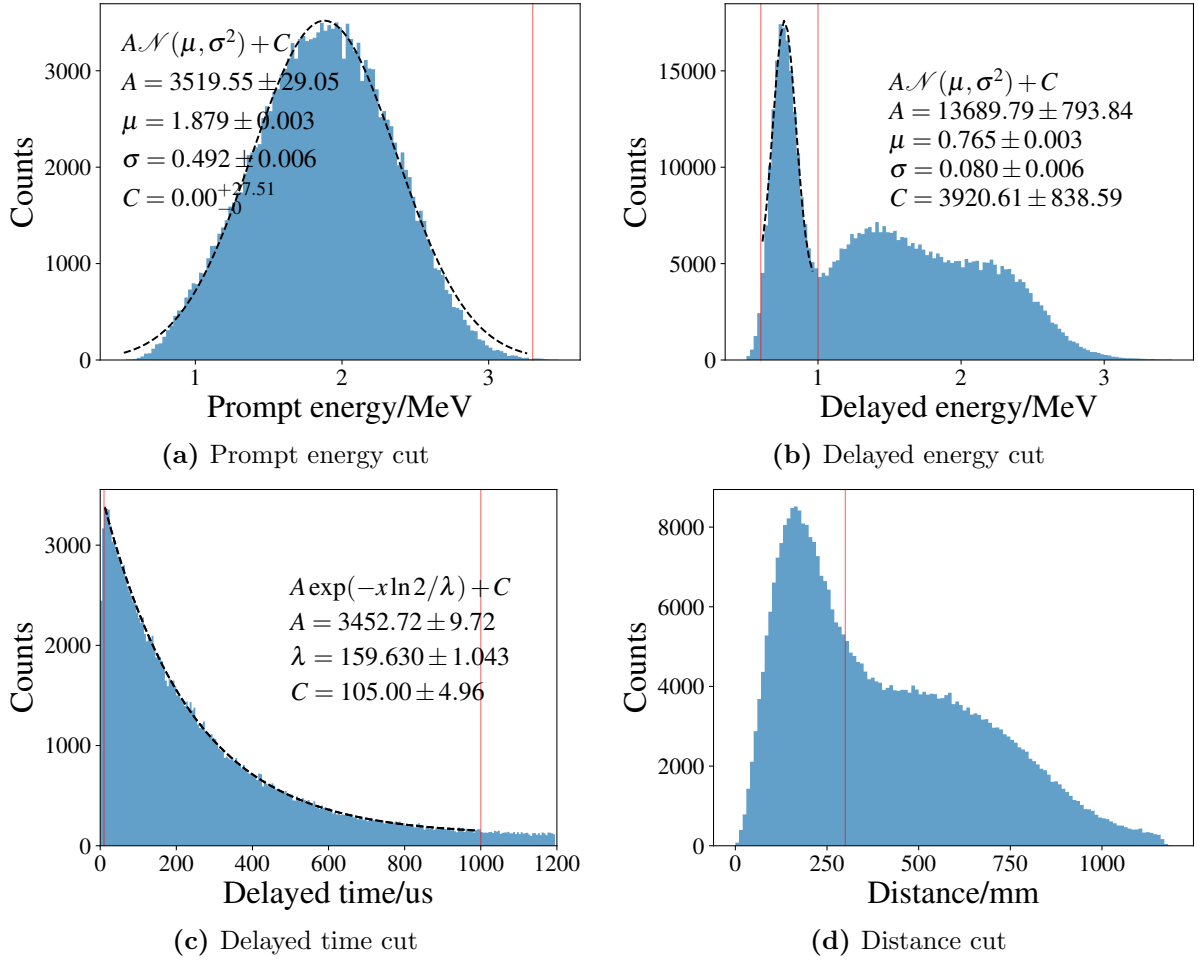


Figure 11: Reconstructions of ^{214}Bi - ^{214}Po cascades in raw data. $\mathcal{N}(\mu, \sigma^2)$ is a Gaussian distribution with the mean μ and variance σ^2 . (a) and (b) is fitted by Gaussian. (c) is fitted by an exponential distribution.

Most backgrounds are gammas from the PMTs. For simplicity, we treat it as a constant. The 25-PMT threshold distorts the beta decay energy spectrum. We use Gaussian to fit the prompt and delayed signals. The average energy of the e^- is approximately ~ 1.879 MeV, and the α peaks at 0.765 MeV due to the ionization quenching. The fitted half-life is close to the true value (164.3 us). The results show that most selected events are cascade signals and our reconstruction works well.

5 Discussion

5.1 Other reflections by acrylic shell

The closer PMT often has a larger gradient in the likelihood function. We select the three closest PMTs in section 3.2 since they are more sensitive to vertex positions. In inhomogeneous materials, normal reflections other than TR at the media boundary focus light, making

predicted PEs peak at some regions that are otherwise as dim as their neighbors. Such focal points and lines are sources to multimodality in the likelihood function.

When the vertices $r/r_{\text{LS}} \in [0.4, 0.5]$, figure 12a (top) shows the photons reflected by the acrylic shell are focused at $\cos \theta \simeq -1$. We record θ_{acr} , which is the central angle defined by the vertex and the point of incidence to the acrylic shell, and compare the θ_{acr} 's distribution of blue PMT at $\theta \simeq 0$ and black PMT at $\theta \simeq \pi$. In figure 12a (bottom), most photons hit the blue PMT directly, but quite a lot of photons bounce to the black PMT after reflection by the acrylic shell. $r = 0.4r_{\text{LS}}$ is therefore denoted as the *focus region*. In figure 12b, the slice of the predicted PE at $r = 0.4r_{\text{LS}}$ peaks at $\cos \theta \simeq -1$, introducing degeneracy of PE predictions. It is also observed at the Borexino CTF [38]. The dashed horizontal line drawn at the abnormal $\cos \theta \simeq -1$ peak intersects with the PE prediction line, which defines a *degenerate region*.

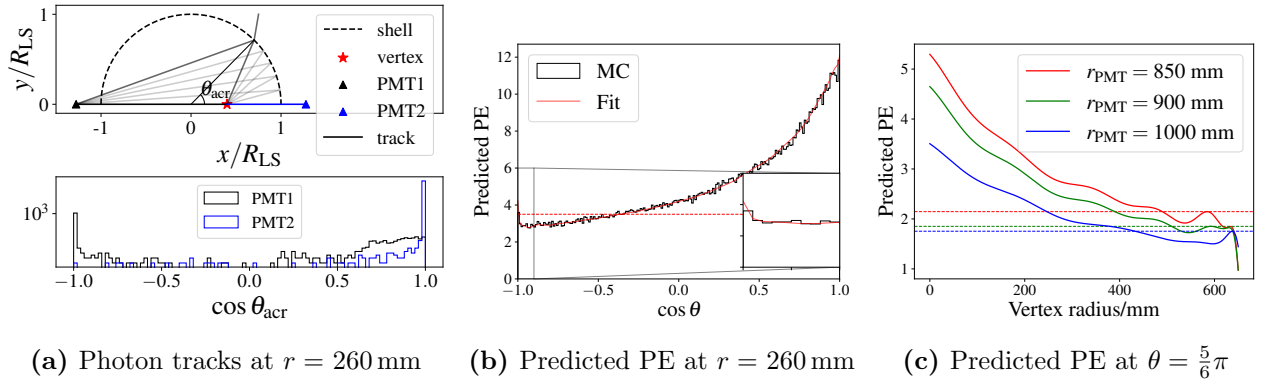


Figure 12: Focus effect at $r = 0.4r_{\text{LS}} = 260$ mm. The tracks of detected photons are sketched in (a). The top of (a) defines θ_{acr} of the tracks. The vertex is relative to PMT1 at $\cos \theta_1 = -1$ and PMT2 at $\cos \theta_2 = 1$. The bottom of (a) is the log-scale distribution of $\cos \theta_{\text{acr}}$. (b) is a slice of $r = 0.4r_{\text{LS}}$ shown in figure 4c. “MC” is the histogram of the simulated events, and “Fit” represents the fitted response in section 2. The inlet zooms in the peak at $\cos \theta = -1$. (c) is the predicted PE at $\theta = 5\pi/6$ conditioned to different r_{PMT} . Each dashed line in (b) and (c) covers a degenerate region.

The opposite PMT plays an important role in the focus region. Vertex reconstruction at $r \sim 260$ mm of simulated events from the Jinping prototype is shown in figure 13a. The hotspots in the zenith θ_v and azimuth ϕ_v map coincide with the PMT-center directions. Our speculation is verified by masking out one PMT in eq. (11), resulting in figure 13b. The hotspot disappears around the masked PMT.

For $r > 0.8r_{\text{LS}}$, photons can reflect multiple times. Figure 12c takes the slice of $\theta = 5\pi/6$ as an example. The superposition of multiple reflections makes the predicted PE peak at around $r > 0.8r_{\text{LS}}$, causing degeneracy. The two local solutions of figure 6c coincides with the degenerate region of the $r_{\text{PMT}} = 900$ mm in figure 12c. Evident in figure 4c, such a multiple-reflection region forms a belt, unfortunately it is no longer possible to select out 3 PMTs to derive a simple criterion.

Generally speaking, degeneracy is inevitable for inhomogeneous materials. Each PMT contributes a specific degenerate region to the likelihood function. For example, vertices around $r = 0.5r_{\text{LS}}$ could degenerate with both the focus region and the TR region simultaneously. The situation is further complicated by the fluctuations on every PMT. Luckily, if the degeneracy scale is less than the vertex resolution, the reconstruction result is effectively not ambiguous anymore. Higher PMT coverage gives a larger slope in the predicted PEs, narrowing the degenerate region, as illustrated by the $r_{\text{PMT}} = 850$ mm line in figure 12c. Therefore

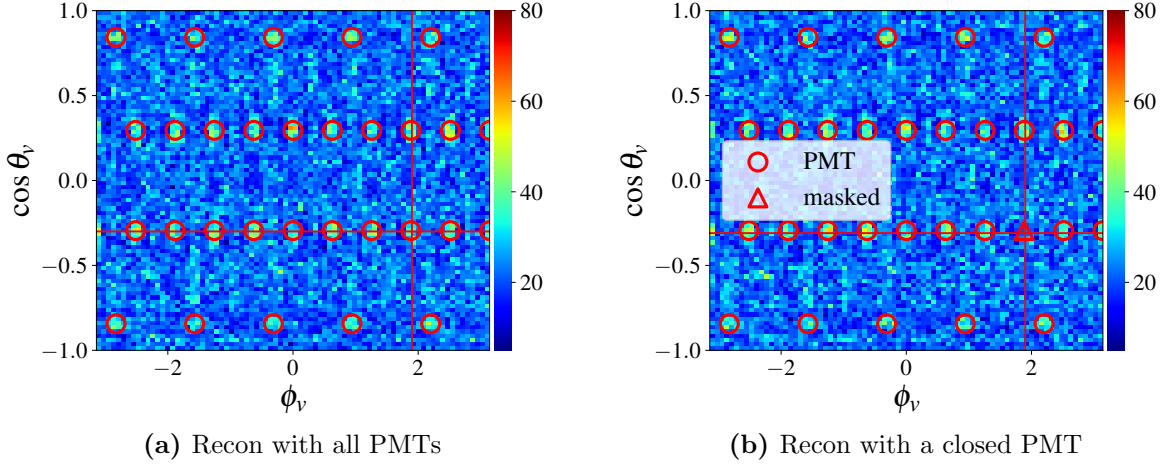


Figure 13: Vertex reconstruction results at $r = 260$ mm subjected to the focus effect. The color is the count of the reconstructed vertices. (a) is the θ_v - ϕ_v map of the vertex reconstruction results in spherical coordinates. The circles indicate the PMT-center directions. (b) is the reconstruction masking out the triangle PMT, noted as “masked”.

we recommend a small r_{PMT} at the lower limit in figure 9b.

5.2 Breaking of spherical symmetry

In figure 10f, energy reconstruction using true vertices “Fit(TrueV)” is still biased when $r = 620$ mm at z axis. Due to the outlet in figure 3, only a small fraction of the photons can be detected in the outlet direction compared to the general direction.

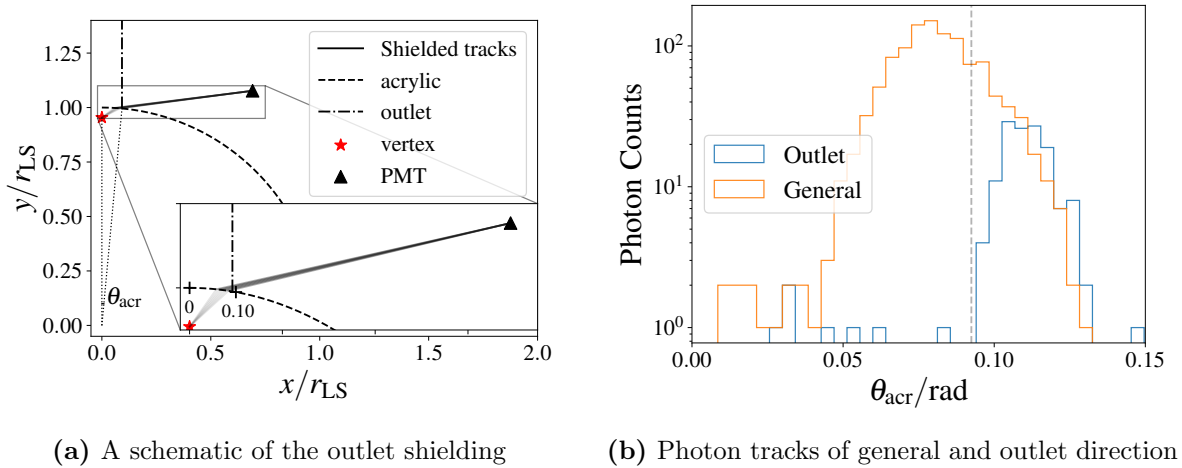


Figure 14: (a) Vertices are at $r = 620$ mm. The *shielded tracks* are the detected tracks in the general direction but not in the outlet direction. The numbers in the zoom axis show the θ_{acr} ’s value in radians. (b) The outlet region is on the left side of the grey dashed line. The distribution of the θ_{acr} of the outlet and general directions are noted as “Outlet” and “General”.

In figure 14a, the outlet breaks spherical symmetry. Figure 14b compares the θ_{acr} distributions of the outlet and general directions. Photons with $\theta_{\text{acr}} < 0.10$ rad are trapped into the outlet and seldomly detected by any PMT.

5.3 Cosine distance for timing

In section 3.1, we ignore the timing information since PE is dominant in the Jinping Prototype. We can expand the vector Λ to include timing for large detectors. The input is the average function $\lambda_i R_i(t)$ of the inhomogeneous Poisson process on each PMT. For continuous form, the d_{cos} is

$$d_{\text{cos}} [\lambda_i(\mathbf{r}_1)R_i(t; \mathbf{r}_1) | \lambda_i(\mathbf{r}_2)R_i(t; \mathbf{r}_2)] = 1 - \frac{\sum_i \int \lambda_i(\mathbf{r}_1)R_i(t; \mathbf{r}_1)\lambda_i(\mathbf{r}_2)R_i(t; \mathbf{r}_2)dt}{\sqrt{\sum_i \int [\lambda_i(\mathbf{r}_1)R_i(t; \mathbf{r}_1)]^2 dt} \sqrt{\sum_i \int [\lambda_i(\mathbf{r}_2)R_i(t; \mathbf{r}_2)]^2 dt}}. \quad (22)$$

5.4 Upgrading Jinping Prototype

The criterion in section 3.3 is a guideline for future detectors. Due to the space limits, PMT coverage over 40% is difficult to achieve at a small radius. Vertices in the central and the TR region make a huge difference in energy reconstruction. If we focus on the most severe degeneracy at the detector center and 600 mm on the z -axis, the main problem is that the gap between PMT1 and PMT3 is too large, as shown in figure 8d. Vertices at the bisector of the 1st and 2nd closest PMTs are in the TR regions of both PMTs. Therefore the criterion could be updated to “the TR regions of the neighboring PMTs do not overlap”. Compared to the criterion in section 3.2 and figure 9b where the vertices are in the PMT-center direction, the updated minimum number of the PMTs relaxes to 1/2 in a two-dimensional slice and 1/4 in three dimensions. It shows that a minimum of 30 PMTs could meet the demand, but should be uniformly distributed. In the current 30-PMT arrangement, 0-to-600 mm large degeneracy is caused by the absence of PMTs in the outlet direction, a big non-uniformity. The Jinping Neutrino Experiment collaboration (JNE) plans to upgrade the prototype to 60 PMTs and narrow the gaps between the PMTs around the outlet.

6 Conclusion

We obtain an accurate detector response model using regression, in which the number of parameters is determined by validation. Compared to purely optics-motivated models inevitably biased at the TR regions and data-driven ones overwhelmed by the degrees of freedom, our model achieves an optimal balance. It is shown to be unbiased in the TR regions while keeping the model complexity under control. For 2 MeV e^- Jinping prototype simulation, the vertex resolution is 60 mm at the center and 20 mm at the TR region except those around the outlet. The energy resolution is $11\%/\sqrt{E[\text{MeV}]}$. The method is confirmed to work on Jinping prototype raw data by ^{214}Bi - ^{214}Po analysis. We believe our construction suits all the spherical detectors, especially handles the optical complexity of those with the TR.

We investigate the reconstruction degeneracy at the Jinping prototype, and confirm its origin to be the multimodality in likelihood functions. With a set of carefully chosen approximations, we derive a necessary condition for a detector to be free from reconstruction degeneracy: the expected PE ratio between the 2 closest PMTs of any event should be less than 10. The criterion is justified by comparing the Jinping prototype and an ideal detector setup. That simple degeneracy criterion marks the first thorough and systematic study on the mis-reconstruction of LS detectors known to us. It guides the upgrade of the Jinping prototype and hopefully will serve as a valuable reference for the design of PMT configurations at

future LS detectors.

Acknowledgments

We appreciate the development of the simulation tool of JSAP by Linyan Wan, Ziyi Guo and Lei Guo. Many thanks to the efforts in the waveform reconstruction by Aiqiang Zhang and Dacheng Xu. We are also grateful to Wentai Luo and Xuwei Liu for discussions on reconstruction. The PMT arrangement is inspired by Bohan Qi. The Corresponding author would like to thank the XMASS collaboration for facilitating the idea of detector response modeling by spherical harmonics. The early seed of this paper roots in exciting discussions with Professors Shiro Ikeda, John Gregory Learned, Kai Uwe Martins and Yoichiro Suzuki. We also thank the Jinping Neutrino Experiment collaboration for sharing the data from the Jinping 1-ton prototype. This work was supported in part by the National Natural Science Foundation of China (No. 12127808 and 12141503) and the Key Laboratory of Particle and Radiation Imaging (Tsinghua University).

References

- [1] BOREXINO collaboration, *Science and technology of Borexino: a real-time detector for low energy solar neutrinos*, *Astroparticle Physics* **16** (2002) 205.
- [2] KAMLAND collaboration, *Precision Measurement of Neutrino Oscillation Parameters with KamLAND*, *Phys. Rev. Lett.* **100** (2008) 221803.
- [3] SNO+ collaboration, *Current Status and Future Prospects of the SNO+ Experiment*, *Adv. High Energy Phys.* **2016** (2016) 6194250 [1508.05759].
- [4] JUNO collaboration, *JUNO physics and detector*, *Prog. Part. Nucl. Phys.* **123** (2022) 103927 [2104.02565].
- [5] JUNO collaboration, *Neutrino Physics with JUNO*, *Journal of Physics G: Nuclear and Particle Physics* **43** (2016) 030401.
- [6] JUNO collaboration, *JUNO physics and detector*, *Progress in Particle and Nuclear Physics* **123** (2022) 103927.
- [7] KAMLAND-ZEN collaboration, *Search for majorana neutrinos near the inverted mass hierarchy region with kamland-zen*, *Phys. Rev. Lett.* **117** (2016) 082503.
- [8] KAMLAND-ZEN collaboration, *First Search for the Majorana Nature of Neutrinos in the Inverted Mass Ordering Region with KamLAND-Zen*, [arXiv:2203.02139](https://arxiv.org/abs/2203.02139).
- [9] SNO+ collaboration, *The SNO+ experiment*, *JINST* **16** (2021) P08059 [2104.11687].
- [10] J. F. Beacom, S. Chen, J. Cheng, S. N. Doustimotlagh, Y. Gao, S.-F. Ge et al., *Letter of Intent: Jinping Neutrino Experiment*, *Chinese Phys. C* **41** (2017) 023002.
- [11] Q. Liu, M. He, X. Ding, W. Li and H. Peng, *A vertex reconstruction algorithm in the central detector of JUNO*, *Journal of Instrumentation* **13** (2018) T09005–T09005.

- [12] H. S. Kim, *Finding an Event Vertex by Using a Weighting Method at RENO*, *New Phys. Sae Mulli* **62** (2012) 631.
- [13] Z. Li, Y. Zhang, G. Cao, Z. Deng, G. Huang, W. Li et al., *Event vertex and time reconstruction in large-volume liquid scintillator detectors*, *Nuclear Science and Techniques* **32** (2021) 1.
- [14] CHOOZ collaboration, *Search for neutrino oscillations on a long baseline at the CHOOZ nuclear power station*, *Eur. Phys. J. C* **27** (2003) 331 [[hep-ex/0301017](#)].
- [15] BOREXINO collaboration, *Borexino calibrations: hardware, methods, and results*, *Journal of Instrumentation* **7** (2012) P10018–P10018.
- [16] O. Tajima, *Measurement of electron anti-neutrino oscillation parameters with a large volume liquid scintillator detector*, *KamLAND*, 2003.
- [17] C. Galbiati and K. McCarty, *Time and space reconstruction in optical, non-imaging, scintillator-based particle detectors*, *Nuclear Instruments and Methods in Physics Research Section A: Accelerators, Spectrometers, Detectors and Associated Equipment* **568** (2006) 700.
- [18] RENO collaboration, *RENO: An Experiment for Neutrino Oscillation Parameter θ_{13} Using Reactor Neutrinos at Yonggwang*, [arXiv:1003.1391](#).
- [19] G. Huang, Y. Wang, W. Luo, L. Wen, Z. Yu, W. Li et al., *Improving the energy uniformity for large liquid scintillator detectors*, *Nucl. Instrum. Meth. A* **1001** (2021) 165287 [[2102.03736](#)].
- [20] Z. Qian, V. Belavin, V. Bokov, R. Brugnera, A. Compagnucci, A. Gavrikov et al., *Vertex and energy reconstruction in JUNO with machine learning methods*, *Nuclear Instruments and Methods in Physics Research Section A: Accelerators, Spectrometers, Detectors and Associated Equipment* (2021) 165527.
- [21] T. Hastie, R. Tibshirani and J. Friedman, *The Elements of Statistical Learning: Data Mining, Inference, and Prediction*. Springer New York, 2013.
- [22] J. A. Nelder and R. W. M. Wedderburn, *Generalized linear models*, *Journal of the Royal Statistical Society. Series A (General)* **135** (1972) 370.
- [23] C. Davino, M. Furno and D. Vistocco, *Quantile Regression: Theory and Applications*. Wiley, 2013.
- [24] R. J. Noll, *Zernike polynomials and atmospheric turbulence*, *JOsA* **66** (1976) 207.
- [25] S. Agostinelli, J. Allison, K. Amako, J. Apostolakis, H. Araujo, P. Arce et al., *Geant4—a simulation toolkit*, *Nuclear Instruments and Methods in Physics Research Section A: Accelerators, Spectrometers, Detectors and Associated Equipment* **506** (2003) 250.
- [26] Z. Wang, Y. Wang, Z. Wang, S. Chen, X. Du, T. Zhang et al., *Design and analysis of a 1-ton prototype of the Jinping Neutrino Experiment*, *Nuclear Instruments and Methods in Physics Research Section A: Accelerators, Spectrometers, Detectors and Associated Equipment* **855** (2017) 81.

- [27] Á. González, *Measurement of areas on a sphere using Fibonacci and latitude–longitude lattices*, *Mathematical Geosciences* **42** (2010) 49.
- [28] Z. Guo, M. Yeh, R. Zhang, D.-W. Cao, M. Qi, Z. Wang et al., *Slow liquid scintillator candidates for MeV-scale neutrino experiments*, *Astroparticle Physics* **109** (2019) 33.
- [29] JNE collaboration, *Measurement of muon-induced neutron production at China Jinping Underground Laboratory*, *Chinese Physics C* (2022) .
- [30] D. Kraft, *A software package for sequential quadratic programming*. Tech Rep DFVLR-FB 88-28, 1988.
- [31] JUNO collaboration, *TAO Conceptual Design Report: A Precision Measurement of the Reactor Antineutrino Spectrum with Sub-percent Energy Resolution*, [arXiv:2005.08745](https://arxiv.org/abs/2005.08745).
- [32] XMASS collaboration, *XMASS detector*, *Nuclear Instruments and Methods in Physics Research Section A: Accelerators, Spectrometers, Detectors and Associated Equipment* **716** (2013) 78.
- [33] XMASS collaboration, *Development of low radioactivity photomultiplier tubes for the XMASS-I detector*, *Nuclear Instruments and Methods in Physics Research Section A: Accelerators, Spectrometers, Detectors and Associated Equipment* **922** (2019) 171.
- [34] W. H. Richardson, *Bayesian-based iterative method of image restoration*, *JoSA* **62** (1972) 55.
- [35] D. C. Xu, B. D. Xu, E. J. Bao, Y. Y. Wu, A. Q. Zhang, Y. Y. Wang et al., *Towards the ultimate PMT waveform analysis for neutrino and dark matter experiments*, *Journal of Instrumentation* **17** (2022) P06040.
- [36] S. Kullback and R. A. Leibler, *On information and sufficiency*, *The annals of mathematical statistics* **22** (1951) 79.
- [37] A. Basu, I. R. Harris, N. L. Hjort and M. C. Jones, *Robust and efficient estimation by minimising a density power divergence*, *Biometrika* **85** (1998) 549.
- [38] BOREXINO collaboration, *Light propagation in a large volume liquid scintillator*, *Nuclear Instruments and Methods in Physics Research Section A: Accelerators, Spectrometers, Detectors and Associated Equipment* **440** (2000) 360.